

Temperature dependent magnetization reversal process of a Ga-doped Nd-Fe-B sintered magnet based on first-order reversal curve analysis

著者	Satoshi Okamoto, Kazunori Miyazawa, Takahiro Yomogita, Nobuaki Kikuchi, Osamu Kitakami, Kentaro Toyoki, David Billington, Yoshinori Kotani, Tetsuya Nakamura, Taisuke Sasaki, Tadakatsu Ohkubo, Kazuhiro Hono, Yukio Takada, Takashi Sato, Yuji Kaneko, Akira Kato
journal or publication title	Acta Materialia
volume	178
page range	90-98
year	2019-10-01
URL	http://hdl.handle.net/10097/00133200

doi: 10.1016/j.actamat.2019.08.004

Temperature dependent magnetization reversal process of a Ga-doped Nd-Fe-B sintered magnet based on first-order reversal curve analysis

Satoshi Okamoto^{1,2}, Kazunori Miyazawa¹, Takahiro Yomogita¹, Nobuaki Kikuchi¹, Osamu Kitakami¹, Kentaro Toyoki^{2,3}, David Billington^{2,3}, Yoshinori Kotani³, Tetsuya Nakamura^{2,3}, Taisuke Sasaki², Tadakatsu Ohkubo², Kazuhiro Hono², Yukio Takada⁴, Takashi Sato⁴, Yuji Kaneko⁴, and Akira Kato⁵

¹Institute of Multidisciplinary Research for Advanced Materials (IMRAM), Tohoku University, Sendai 980-8577, Japan

²Elements Strategy Initiative Center for Magnetic Materials (ESICMM), National Institute for Materials Science (NIMS), Tsukuba 305-0047, Japan

³Japan Synchrotron Radiation Research Institute (JASRI), Sayo 679-5198, Japan

⁴Toyota Central R&D Labs., Inc., 41-1, Nagakute 480-1192, Japan

⁵Toyota Motor Corp, Advanced Material Engineering Div., Susono 410-1193, Japan

Abstract

A Ga-doped Nd-Fe-B sintered magnet has attracted significant attention as a heavy-rare-earth-free high-performance magnet. We have studied the temperature dependent magnetization reversal process of a Ga-doped Nd-Fe-B sintered magnet based on the first-order reversal curve (FORC) analysis. The FORC diagram pattern of the Ga-doped Nd-Fe-B sintered magnet changes from single spot in the high field region at room temperature to double spots in the low and high field regions at 200 °C, indicating that the dominant magnetization reversal process changes from single domain type to multidomain type. The single domain magnetization reversal at room temperature is well confirmed by using the soft X-ray magnetic circular dichroism microscopy observation. This change in the magnetization reversal process is well discussed by the temperature dependent local demagnetization field and the saturation field of multidomain state. Moreover, we have demonstrated the quantitative analysis of the FORC diagram pattern, which makes a deeper understanding of the magnetization reversal process of the Ga-doped Nd-Fe-B sintered magnet.

1 Introduction

During the past decade, the development of a high-performance Nd-Fe-B magnet without adding heavy-rare earth elements has been one of the crucial issues in the field of permanent magnets. It has been known that a small amount of Ga addition effectively enhances the coercivity of Nd-Fe-B sintered magnets [1-3]. Recently, an optimally annealed Ga-doped Nd-rich Nd-Fe-B sintered magnet, hereafter referred as a Ga-doped Nd-Fe-B magnet for simplicity, has attracted significant attention as one of the solutions for this issue [4-6]. This magnet presents some unique features compared with conventional Nd-Fe-B sintered magnets. The coercivity μ_0H_c of the as-sintered Ga-doped Nd-Fe-B magnet is about 1 T, and increases to 1.8 T after annealing at the optimum temperature of 480 °C [5]. The increment of μ_0H_c after the optimum annealing is 80 %, which is much larger than that of about 20 % in conventional Nd-Fe-B sintered magnets. Very recently, Sasaki *et al.* have revealed that these different behaviors of μ_0H_c against annealing is attributed to the different grain boundary (GB) phase formations between the conventional and Ga-doped Nd-Fe-B magnets [5,7,8].

The GB phases in conventional Nd-Fe-B magnets are assigned to crystalline and amorphous ones. The former is mainly found along the *c*-plane, and its Nd content is higher than 60 at. %. On the other hand, the latter exists along the *ab*-plane with much lower Nd content of about 35 at. % [7]. This low Nd content amorphous GB phase has been verified as ferromagnetic [9-12], indicating that the inter-grain exchange coupling is non-trivial.

In Ga-doped Nd-Fe-B magnets, there are three types triple junction (TJ) phases, that is, $\text{Nd}_6\text{Fe}_{13}\text{Ga}$, $\text{Ia}\bar{3}$, and amorphous phases [5,8]. Latter two TJ phases are non-magnetic because of their very high Nd content. The TJ phase of $\text{Nd}_6\text{Fe}_{13}\text{Ga}$ has Fe rich content, however, it is predicted as antiferromagnetic from the first-principles calculation [13]. In the as-sintered Ga-doped Nd-Fe-B magnet, the isolation of $\text{Nd}_2\text{Fe}_{14}\text{B}$ main phase grain is imperfect due to the insufficient growth of the GB phases. After the optimum annealing, the GB phases become very clear, and their chemical compositions and structures are identical to their connecting TJ phases [8]. This fact evidences that the TJ phases infiltrate into the surrounding GB. Moreover, all these GB phases are verified as non-ferromagnetic from the elaborate electron holography study [14]. Therefore, the large enhancement of μ_0H_c in the optimally annealed Ga-doped Nd-Fe-B magnets is attributed to the inter-grain exchange decoupling due to the formation of non-ferromagnetic GB phases. Previously, it has been discussed that the formation of $\text{Nd}_6\text{Fe}_{13}\text{Ga}$ phase has a strong correlation with the large enhancement of μ_0H_c [15,16]. However, although the $\text{Nd}_6\text{Fe}_{13}\text{Ga}$ phase is one of the non-ferromagnetic TJ and GB phases, it is not essential for the large μ_0H_c

in Ga-doped Nd-Fe-B magnets [17].

These changes in the GB phases between the conventional and Ga-doped Nd-Fe-B magnets also affect the magnetization reversal process. Soderžnik *et al.* reported that cascade magnetization reversal was dominant in the conventional Nd-Fe-B magnet, whereas it was severely suppressed in the optimally annealed Ga-doped Nd-Fe-B magnet from the magneto-optical Kerr effect (MOKE) microscopy observations [6]. These different magnetization reversal processes can be understood as consequences of the different inter-grain exchange couplings in these two magnets. However, it is hard to fully understand the magnetization reversal process of the Ga-doped Nd-Fe-B magnet only from the MOKE microscopy since the information from the MOKE microscopy is limited to the surface. Moreover, the surface of the magnet is inevitably damaged during the mechanical polishing process which is required for the MOKE observation.

Very recently, we have successfully demonstrated that the first-order reversal curve (FORC) analysis is a potential method for analyzing the magnetization reversal processes of Nd-Fe-B sintered magnets [18]. The magnetization reversal curve is taken with the field H starting from a certain reverse field H_r on the demagnetization curve. These reversal curves are sequentially taken with changing H_r , and consequently, the inside of the major magnetization hysteresis curve is filled with the reversal curves. Each point of magnetization m on the reversal curve is a function of H and H_r , and the FORC distribution ρ is defined as the second-order derivative of m with respect to H and H_r , as follows:

$$\rho(H, H_r) = -\frac{\partial}{\partial H_r} \left(\frac{\partial m}{\partial H} \right). \quad (1)$$

The contour map of ρ as function of H and H_r is called as the FORC diagram [19,20]. So far, the FORC analysis has been applied to many magnetic materials [21-30], and most of them have been analyzed under the assumption of the Preisach model [19], in which the magnetic material is considered to consists of many hysteresis units called as hysterons. In our previous study, however, we have demonstrated that the straightforward adoption of this model is not adequate for Nd-Fe-B sintered magnets, and we have alternatively proposed to analyze the FORC diagram of Nd-Fe-B sintered magnets based on the definition of ρ in eq. (1) [18]. Eq. (1) represents that ρ is the derivation of the magnetic susceptibility ($\partial m / \partial H$). Thus, the FORC diagram visualizes the change in the magnetic susceptibility on the field plane of (H, H_r) . A commercial Nd-Fe-B sintered magnet typically exhibits a FORC diagram pattern with two remarkable spots, one in the low-field and the other in the high-field region. The high-field FORC spot corresponds to the large magnetic susceptibility state at the coercivity, while the low-field FORC spot evidences the presence of high magnetic susceptibility state in the low-field region. These low-field and high-field FORC

spots of a Nd-Fe-B sintered magnet have been commonly reported [31-33]. Soft X-ray magnetic circular dichroism (XMCD) microscopy was used to examine the magnetization reversal processes corresponding to these two FORC spots [18]. As a result, the large magnetic susceptibility states of the low-field and high-field FORC spots were attributed to the magnetization reversals of multidomain (MD) and single domain (SD) grains, respectively. Thus, it is concluded that the demagnetization process of the commercial Nd-Fe-B sintered magnet is initiated by the MD magnetization reversal followed by the SD magnetization reversal. Moreover, the MD magnetization reversal becomes dominant with increasing the temperature.

In this study, we have adopted the FORC analysis to the as-sintered and annealed Ga-doped Nd-Fe-B magnets, and their different magnetization reversal processes are investigated in detail. From the FORC analyses, we have clearly verified that the SD magnetization reversal is dominant in the annealed Ga-doped Nd-Fe-B magnet at room temperature (RT) whereas the MD magnetization reversal is dominant in the as-sintered one. The SD magnetization reversal in the annealed Ga-doped Nd-Fe-B magnet is well confirmed by the XMCD microscopy observation. However, the MD magnetization reversal becomes dominant in the annealed Ga-doped Nd-Fe-B magnet at an elevated temperature. This change in the magnetization reversal process against temperature is discussed from the local demagnetization field and the saturation field of MD state. Finally, we have attempted the quantitative analysis of FORC diagram pattern of the Ga-doped Nd-Fe-B magnet, which offers more detailed information on the magnetization reversal process.

2 Experimental

Two magnet samples of as-sintered and optimally annealed Ga-doped Nd-Fe-B magnets are studied. The nominal composition of the magnets is $\text{Fe}_{77.1}\text{Nd}_{11.6}\text{Pr}_{3.7}\text{B}_{5.1}\text{Cu}_{0.1}\text{Co}_{1.0}\text{Al}_{0.9}\text{Ga}_{0.5}$ in at. %, which is slightly rich in rare-earth elements, and doped with a small amount of Ga of 0.5 at. %. The microstructures of these magnets were well studied in ref. [5,8]. The major demagnetization and reversal curves of the magnets were measured using a vibrating sample magnetometer (VSM) with a maximum magnetic field of 2.6 T. The measurement temperature was varied from RT to 200 °C. To avoid the extrinsic deformation of FORC diagram pattern owing to the macroscopic demagnetization field [32,34], the samples used for FORC measurements were shaped into a pillar of 0.5 mm in width and 3 mm in length with their long axes along the magnetic easy axes of the magnets [18,35], resulting in the very small macroscopic demagnetization factor N_z of 0.04. The magnetic field was applied along the long axis of the pillar.

The XMCD microscopy observations under the similar field sequence of FORC measurements were performed at the soft X-ray beamline of BL25SU in SPring-8

[12,18,36,37]. Measurements were conducted at RT, and the X-ray absorption signal was detected using a total electron yield method at the Fe L₃ (707.9 eV) edge. The detailed measurement conditions are the same as those described in ref. [18]. The pillar-shaped magnet sample was fractured in a high vacuum condition ($\sim 3 \times 10^{-6}$ Pa) of the sub-chamber of the XMCD measurement system, and then it was promptly transferred into the main chamber ($< 5 \times 10^{-7}$ Pa). After the fracturing, the sample shape was 0.5 mm in width and 3.5 mm in length, resulting in N_z of 0.03. The fracturing is preferentially taken place at the thin GB phase rather than the Nd₂Fe₁₄B main phase grain, consequently, most the grains on the fractured surface are covered with the very thin GB phase without having any mechanical damages. It was confirmed that the magnetization curve of the commercial Nd-Fe-B sintered magnet obtained using XMCD measurement was identical to that obtained using VSM [12,18]. These surface grains are referred as inter-grain fractured grains. Some grains take intra-grain fracturing. These inter-grain and intra-grain fractured grains are easily discriminated in a chemical contrast image using the absorption intensity ratio of the Fe L₃ and Nd M₄ edges [18,37].

3 Results and discussion

3.1 FORC measurements

Figure 1 shows the coercivity $\mu_0 H_c$ of the as-sintered and annealed Ga-doped Nd-Fe-B magnets as a function of temperature T . The value of $\mu_0 H_c$ of the as-sintered magnet is 0.6 T at RT, and it significantly increases up to 1.7 T after annealing. Then, it monotonically decreases with increasing the temperature. The values of $\mu_0 H_c$ at RT are slightly smaller than those reported in ref. [5] (1 and 1.8 T for the as-sintered and annealed Ga-doped Nd-Fe-B magnets, respectively) even though the magnets are the same. This is probably due to the different macroscopic demagnetization fields, which is resulted from the different sample shapes used in these two works.

Figures 2(a) and 2(b) show the reversal curves and FORC diagram of the as-sintered Ga-doped Nd-Fe-B magnet at RT. The FORC diagram pattern of the as-sintered magnet exhibits the low-field and high-field FORC spots highlighted by the blue and red lines in Fig. 2(b), respectively, and these corresponding large magnetic susceptibility regions on the reversal curves are also highlighted in Fig. 2(a). These two FORC spots have been commonly observed in the conventional Nd-Fe-B sintered magnets [18,31-33]. The high-field FORC spot obviously corresponds to the large susceptibility state at the coercivity, while the low-field FORC spot corresponds to the large susceptibility state in the vicinity of the zero-field region. The reversal curve corresponded to the low-field FORC spot starts from $\mu_0 H_r$ at around $\mu_0 H_c$, whereas that for the high-field FORC spot is traced from $\mu_0 H_r$ much larger than $\mu_0 H_c$. According to our previous study [18], these low-field and high-field FORC spots

correspond to the MD and SD magnetization reversals, respectively. Therefore, the demagnetization process of the as-sintered Ga-doped Nd-Fe-B magnet is initiated by the MD magnetization reversal, and then the SD magnetization reversal takes place near the saturation. Here, it should be addressed that the position of the high-field FORC spot is underneath the diagonal line of $H = -H_r$, reflecting that the high-field FORC spot requires $\mu_0 H_r$ much larger than $\mu_0 H_c$. Moreover, the shape of the high-field FORC spot is obliquely prolonged. The prolonged shape of the high-field FORC spot reflects the H_r dependent coercivity, as will be discussed in section 4.

Figures 3(a) and 3(b) present the reversal curves and the FORC diagram of the annealed Ga-doped Nd-Fe-B magnet at RT, respectively. Contrary to the FORC diagram of the as-sintered magnet shown in Fig. 2(b), only the high-field FORC spot highlighted by the red line is detected in Fig. 3(b), and its position is very close to the diagonal line of $H = -H_r$. These results indicate that the SD magnetization reversal, which mainly occurs at $-H_r \approx H_c$, is dominant in the annealed Ga-doped Nd-Fe-B magnet at RT. These results are in good agreement with the recent MOKE microscopy observations [6]. This SD magnetization reversal would be attributed to the inter-grain exchange decoupling nature of this magnet. With increasing the temperature, however, these features of the FORC diagram dramatically change as shown in Figs. 3(c)-3(f). The low-field FORC spot becomes visible, and the position of the high-field FORC spot deviates from the diagonal line of $H = -H_r$ at 100 °C (Figs. 3(c) and 3(d)). These changes become more significant at 200 °C (Figs. 3(e) and 3(f)). The low-field FORC spot becomes very strong, and the high-field FORC spot largely deviates from the diagonal line of $H = -H_r$. These results indicate that the MD magnetization reversal becomes dominant at high temperature even in the annealed Ga-doped Nd-Fe-B magnet. Moreover, the shape of the high-field FORC spot at 200 °C is obliquely prolonged, similar to the one observed in the as-sintered magnet shown in Fig. 2(b). These results strongly indicate that the magnetization reversal process does not determined only by the inter-grain exchange coupling. Detailed discussion on this issue will be given in Section 4.

Note that the small kinks are observed in the major demagnetization and reversal curves at $\mu_0 H \approx 0$, which indicates the presence of superficial magnetic damaged layers owing to the mechanical polishing [6,18,38]. While the FORC spot that corresponds to these kinks should have occurred near the origin of the FORC diagram, no remarkable spots are observed near the origins of the FORC diagrams shown in Figs. 3(b), 3(d), and 3(f). Therefore, the kinks only cause the reversible magnetization changes and their effect on the magnetization reversal process of the entire magnet is less significant.

3.2 XMCD microscopy observations

The FORC diagram in Fig. 3(b) illustrates that the SD magnetization reversal is dominant in the annealed Ga-doped Nd-Fe-B magnet at RT. To confirm this SD magnetization reversal, the XMCD microscopy observation is conducted under the field sequence similar to that used for the FORC measurements.

The red dots in Fig. 4(a) show the major XMCD demagnetization curve of the fractured surface of the annealed Ga-doped Nd-Fe-B magnet. For comparison, the black dots in Fig. 4(a) represent the major demagnetization curve obtained using VSM. Figures 4(b)-4(g) show the XMCD images at the magnetic fields corresponding to the encircled data points on the XMCD curve. The grain boundaries are rimmed by black and white lines, which denote the inter-grain and intra-grain fractured grains, respectively. The intra-grain fractured grains tend to be larger than the inter-grain fractured ones. Starting from the positively saturated state at $\mu_0H = 3$ T (Fig. 4(b)), some grains reverse at $\mu_0H = 0$ T (Fig. 4(c)). Subsequently, with decreasing μ_0H up to -2 T, each grain sequentially reverses (Figs. 4(d)-4(g)). At $\mu_0H = 2$ T (Fig. 4(g)), where is the tail region of the demagnetization curve, while most grains negatively reverse, some grains remain lastly. During this reversal process, most grains appeared to reverse as SD state although a few MD grains are found. This is different from that in the commercial Nd-Fe-B magnet, where many MD grains reverse in cascade-like [6,18]. Moreover, contrary to the good agreement between the XMCD and VSM curves in the commercial Nd-Fe-B magnet [12,18], the XMCD curve of the annealed Ga-doped Nd-Fe-B magnet obviously deviates from the VSM one, particularly in the shoulder region of the magnetization curve ($0 \text{ T} > \mu_0H > -2 \text{ T}$ in Fig. 4(a)). This indicates that the fractured surface of the annealed Ga-doped Nd-Fe-B magnet is easily demagnetized compared with the inside of the magnet. This would be understood by the different inter-grain exchange couplings between the commercial and the annealed Ga-doped Nd-Fe-B magnets. In the commercial Nd-Fe-B magnet, the magnetization of the surface grains is supported by the surrounding grains due to the presence of the inter-grain exchange coupling. On the other hand, this support by the surrounding grains is very weak in the annealed Ga-doped Nd-Fe-B magnet due to the inter-grain exchange decoupling, leading to the prompt demagnetization at the surface.

Figure 5(a) presents the XMCD reversal curve of the annealed Ga-doped Nd-Fe-B magnet starting from $\mu_0H_r = -1.6$ T ($\approx \mu_0H_c$), which corresponds to the high-field FORC spot, as indicated by the red dots. For comparison, the black and gray dots denote the reversal curve and the major demagnetization curve measured by VSM, respectively. Figures 5(b)-5(g) are the XMCD images corresponding to the encircled data points on the XMCD reversal curve. Similar to the major demagnetization curve in Fig. 4(a), the XMCD reversal curve also deviates from the VSM reversal curve, particularly in the shoulder region ($0 \text{ T} < \mu_0H < 1.5 \text{ T}$ in Fig. 5(a)). The XMCD image

at $\mu_0 H_r = -1.6$ T exhibits many negatively reversed SD state grains (Fig. 5(b)). Subsequently, with increasing the magnetic field up to 1.8 T, these negatively reversed grains gradually reverse back positively (Figs. 5(c)-5(g)). During this process, whereas some grains become MD state particularly at $\mu_0 H = -0.2$ and 0.2 T (Figs. 5(c) and 5(d)), most grains appear to reverse as SD state.

Figure 6 shows the color maps of the grains that reverse as SD and MD states or remains as unreversed for each reversal curve. Moreover, the histogram of SD, MD, and unreversed grains as a function of $\mu_0 H_r$ is presented. At the beginning of the demagnetization process ($\mu_0 H_r = -0.7$ and -1.1 T), the numbers of SD and MD grains are almost the same, but the diameter of the MD grain tends to be larger than that of the SD grain in this magnetic field range. The number of SD grains rapidly increases from $\mu_0 H_r = -1.6$ T, and the SD grains became dominant. These results clearly demonstrate that the SD magnetization reversal is dominant in the Ga-doped Nd-Fe-B magnet at RT, consisting very well with the FORC diagram pattern with the single high-field spot (Fig. 3(b)). It is very interesting to note that the number of MD grain decreases during the latter half of the demagnetization, indicating that some grains which firstly take MD state converted into SD state during the latter half of the demagnetization process once they are fully saturated. The intra-grain fractured grains tend to take the MD state and easily reverse at the beginning of the demagnetization process. This would be explained by the larger effective local demagnetization field owing to the larger grain size of the intra-grain fractured grains [39].

4. Discussion

4.1 Temperature dependence of magnetization reversal process

As mentioned in Introduction, all the GB phases of the annealed Ga-doped Nd-Fe-B magnet are non-ferromagnetic [5,6,8], indicating the inter-grain exchange decoupling. This well agrees with the sequential magnetization reversal of each grain with SD state observed by XMCD microscopy (Fig. 5). Therefore, someone may say that the SD magnetization reversal in the annealed Ga-doped Nd-Fe-B magnet is the consequence of the inter-grain exchange decoupling. With increasing temperature, however, the FORC diagram pattern changes from single spot to double spots, indicating that the MD magnetization reversal becomes dominant at elevated temperature. Moreover, this double spot FORC diagram pattern is quite similar to that of the as-sintered Ga-doped Nd-Fe-B magnet which has the non-trivial inter-grain exchange coupling. These facts indicate that the inter-grain exchange coupling is not the essential factor for the SD magnetization reversal. Then, let us discuss what is the decisive factor for the SD and MD magnetization reversals in the Ga-doped Nd-Fe-B magnets.

Both the SD and MD magnetization reversals in the Ga-doped Nd-Fe-B magnets are initiated by the nucleation of a small reversed domain because the grain size is much larger than the exchange length of Nd₂Fe₁₄B, which is roughly estimated to be ~4 nm from the Bloch wall width. In this situation, the boundary between the SD and MD magnetization reversals is given to be $H_n/H_s^{\text{MD}} \approx 1$, where H_n and H_s^{MD} are the nucleation and MD saturation fields, respectively. For the condition of $H_n/H_s^{\text{MD}} > 1$, the reversed domain nucleated at H_n is rapidly wiped out, resulting that the SD magnetization reversal is observed. Otherwise the reversed domain remains in the grain, resulting in the MD magnetization reversal.

Roughly saying, H_c is a good measure of H_n . Then, we will propose that H_s^{MD} is evaluated from a remanent initial magnetization curve. Since an initial magnetization curve starts from the thermally demagnetized state, most grains in the magnet initially stay to be MD state. With increasing magnetic field, the domain in each grain moves against the local demagnetization field. Therefore, the saturation field of the initial magnetization curve H_s^i is regarded to be a good measure of the local demagnetization field. However, this is not the MD saturation field H_s^{MD} . If a vestige of the reversed domain remains, it would quickly expand when the magnetic field is removed. This behavior is obviously observed in a remanent initial magnetization curve. Figure 7(a) presents the initial and remanent initial magnetization curves of the annealed Ga-doped Nd-Fe-B magnet at RT. The magnetization value of each data point on the initial magnetization curve largely decreases when the magnetic field is removed, as illustrated in the inset of Fig. 7(a). The remanent initial magnetization curve is obtained by plotting the remanent magnetization value as a function of the magnetic field. The saturation field of the remanent initial magnetization curve H_s^r is much larger than H_s^i , indicating that much larger magnetic field is required to perfectly collapse the vestige of the reversed domain. Thus, H_s^r is considered to be a good measure of H_s^{MD} . Quantitatively estimating H_s^i and H_s^r , however, is not easy, since the initial and remanent initial magnetization curves vary gradually near their saturations. The saturation fields of H_s^i and H_s^r are defined as the crossing points of two lines: the extrapolation from the saturation and the tangent at the point of largest slope change (maximum d^2m/dH^2). Thus determined values of $\mu_0H_s^i$ and $\mu_0H_s^r$ of the as-sintered and annealed Ga-doped Nd-Fe-B magnets are plotted as a function of the temperature as shown in Fig. 7(b). In addition, μ_0H_c is also plotted. For the as-sintered Ga-doped Nd-Fe-B magnet, $\mu_0H_s^r$ is much larger than μ_0H_c at RT, corresponding to the case of $H_n/H_s^{\text{MD}} < 1$. This looks consistent with the conclusion obtained from the FORC diagram in Fig. 2, that is, the MD magnetization reversal is dominant in the as-sintered Ga-doped Nd-Fe-B magnet. On the other hand, the temperature dependence of $\mu_0H_s^i$ and $\mu_0H_s^r$ of the annealed Ga-doped Nd-Fe-B magnet is less significant, whereas the coercivity rapidly decreases with increasing the

temperature. Thus, $\mu_0 H_c$ is much larger than $\mu_0 H_s^r$ at RT, corresponding to the case of $H_n/H_s^{MD} > 1$. However, this relationship becomes inverted for $T \geq 150$ °C. These results are in good agreement with the conclusions obtained from the FORC diagrams of the annealed Ga-doped Nd-Fe-B magnet in Fig. 3, that is, the SD magnetization reversal is dominant at RT, and the MD magnetization reversal becomes dominant at 200 °C in the annealed Ga-doped Nd-Fe-B magnet.

As mentioned above, since H_s^i is considered to be a measure of the local demagnetization field, the small temperature dependence of H_s^i would be very reasonable since the local demagnetization field is proportional with the saturation magnetization which exhibits very small temperature dependence in this temperature range. By contrast, H_s^r exhibits somewhat larger temperature dependence compared with H_s^i , since H_s^r is assumed to consist of the local demagnetization field, which is represented by H_s^i , and the collapsing field of the reversed domain vestige H_s^{col} . Table I summarizes the representative values of $\mu_0 H_s^i$ and $\mu_0 H_s^{col}$ ($= \mu_0 H_s^r - \mu_0 H_s^i$). The temperature variations of $\mu_0 H_s^{col}$ are larger than those of $\mu_0 H_s^i$ because $\mu_0 H_s^{col}$ reflects the domain wall energy [40]. $\mu_0 H_s^{col}$ of the as-sintered Ga-doped Nd-Fe-B magnet is very large compared with those of the annealed magnet. For the as-sintered magnet, the domain wall could move from grain to grain owing to the imperfect grain isolation [5]. Therefore, the largest $\mu_0 H_s^{col}$ among these connected grains might govern the saturation of the entire magnet.

4.2 Quantitative analysis of FORC diagram

Previously, quantitative analysis of FORC diagrams has been studied under the assumption of the Preisach model [19], and the coercivity and interaction field dispersions have been discussed [21-30]. For Nd-Fe-B sintered magnets, however, the analysis based on the Preisach model is not adequate, as discussed in our previous study [18]. Instead, we have qualitatively analyzed the FORC diagram patterns of Nd-Fe-B sintered magnets based on the original definition of FORC distribution ρ (eq. (1)) as discussed in Section 3. Here, we attempt to draw some of quantitative parameters from the FORC diagram based on the original definition of ρ . Figures 8(a) and 8(b) again show the reversal curves and FORC diagram, respectively, of the as-sintered Ga-doped Nd-Fe-B magnet as graphical quantitative analysis examples. The red and blue dots in Fig. 8(b) denote the peak top positions of the high-field and low-field spots, respectively, while their corresponding positions on the reversal curves are also represented by the red and blue dots in Fig. 8(a). The peak fields $\mu_0 H_{p,r}^{L(H)}$ and $\mu_0 H_p^{L(H)}$ along the H_r - and H -axes of the FORC diagram are plotted as a function of temperature T as shown in Figs. 8(c) and 8(d), respectively. The superscripts of L and H denote those of the low-field and high-field FORC spots, respectively. The coercivity $\mu_0 H_c$ is also plotted for comparison. The value of $\mu_0 H_{p,r}^L$

of the as-sintered Ga-doped Nd-Fe-B magnet in Fig. 8(c) is very close to $\mu_0 H_c$, indicating that the low-field FORC spot is attributed to the reversal curve starting from near the coercivity. On the other hand, $\mu_0 H_{p,r}^H$ of the as-sintered Ga-doped Nd-Fe-B magnet is much larger than $\mu_0 H_c$. Both $\mu_0 H_{p,r}^L$ and $\mu_0 H_{p,r}^H$ of the annealed Ga-doped Nd-Fe-B magnet exhibit very large temperature dependences, as well as that of $\mu_0 H_c$. While $\mu_0 H_{p,r}^H$ is very close to $\mu_0 H_c$ at RT, it deviates from $\mu_0 H_c$ at high temperature. By contrast, $\mu_0 H_{p,r}^L$ becomes close to $\mu_0 H_c$ at high temperature. These changes reflect the changes in the magnetization reversal process from the SD magnetization reversal at RT to the MD magnetization reversal at high temperature. While $\mu_0 H_p^H$ of the annealed Ga-doped Nd-Fe-B magnet shown in Fig. 8(d) also exhibits a significant temperature dependence, the values are slightly smaller than $\mu_0 H_c$. Moreover the $\mu_0 H_p^L$ is almost zero regardless of the sample and temperature, indicating that the domain wall in the MD state smoothly propagate by applying very small fields.

The full width at half-maximum (FMHM) along the H_r - and H -axes of the FORC diagram $\mu_0 \Delta H_r^{L(H)}$ and $\mu_0 \Delta H^{L(H)}$, respectively, are depicted in Fig. 8(b), while their corresponding field ranges on the reversal curves are depicted in Fig. 8(a). Thus obtained $\mu_0 \Delta H_r^{L(H)}$ and $\mu_0 \Delta H^{L(H)}$ are plotted as a function of temperature T in Figs. 8(e) and 8(f), respectively. Interestingly, $\mu_0 \Delta H_r^H$ is much larger than $\mu_0 \Delta H_r^L$, and both are almost independent of sample and temperature, as shown in Fig. 8(e). $\mu_0 \Delta H_r^H$ and $\mu_0 \Delta H_r^L$ obviously represent the reversal field distributions of the SD and MD magnetization reversals during the demagnetization process. In particular, $\mu_0 \Delta H_r^H$ involves the tail region near the saturation. According to the XMCD microscopy observations in Fig. 4(g), this tail region corresponds to the magnetization reversals of the lastly remaining grains. Since these remaining grains gradually reverse, $\mu_0 \Delta H_r^H$ becomes much larger than $\mu_0 \Delta H_r^L$. The very small temperature dependences of $\mu_0 \Delta H_r^L$ and $\mu_0 \Delta H_r^H$ suggest that the reversal field distributions of the MD and SD magnetization reversals of the Ga-doped Nd-Fe-B magnet are governed by the local demagnetization field as aforementioned saturation field of the initial magnetization curve.

The values of $\mu_0 \Delta H^L$ and $\mu_0 \Delta H^H$ in Fig. 8(f) represent the magnetizing field ranges of the MD and SD magnetization reversals on the reversal curves, respectively. Unlike $\mu_0 \Delta H_r^L$ in Fig. 8(e), $\mu_0 \Delta H^L$ of the as-sintered Ga-doped Nd-Fe-B magnet at RT is much larger than that of the annealed magnet at high temperature. It is very interesting to note that $\mu_0 \Delta H^H$ of the annealed magnet significantly depends on temperature, but its behavior is obviously different from those of $\mu_0 H_{p,r}^H$ and $\mu_0 H_p^H$, as presented in Figs. 8(c) and 8(d). $\mu_0 \Delta H^H$ largely decreases in the range of RT-100 °C, then it changes very gradually in the range of 100-200 °C. This behavior could be explained by assuming two contributions to $\mu_0 \Delta H^H$, i.e., the coercivity

dispersion and the H_r -dependent coercivity. The former is mainly identified in the annealed Ga-doped Nd-Fe-B magnet at RT. In this case, the high-field spot of the FORC diagram locates very close to the diagonal line of $H = -H_r$ as presented in Fig. 3(b). The latter contribution is mainly found in the as-sintered Ga-doped Nd-Fe-B magnet at RT, as presented in Fig. 2(b) and the annealed magnet at high temperature, as shown in Figs. 3(d) and 3(f), respectively. This contribution causes the obliquely prolonged shape of the high-field FORC spot. As mentioned above, the SD magnetization reversal only appears after the MD states is fully saturated in the as-sintered Ga-doped Nd-Fe-B magnet at RT and annealed magnet at high-temperature. Therefore, the reversal curves for the high-field FORC spot mainly originates from the tail region near the saturation of the demagnetization process. The magnetization reversal in this region is attributed to the lastly remaining grains as confirmed by the XMCD microscopy observation (Figs. 4(g)). Interestingly, the values of $\mu_0\Delta H^H$ of the as-sintered Ga-doped Nd-Fe-B magnet at RT and annealed magnet at high temperature are almost the same, whereas their μ_0H_c are quite different. This fact indicates that the H_r -dependent coercivity might not originate from the magnetically locked pinning mechanism as previously considered [41], but rather from the stray field of the lastly remaining grains in the tail region near the saturation.

5. Summary

We have studied the FORC analysis on the as-sintered and optimally annealed Ga-doped Nd-Fe-B sintered magnets and discussed the temperature dependent magnetization reversal process. The FORC diagram pattern of the as-sintered Ga-doped Nd-Fe-B magnet consisted of low-field and high-field FORC spots, which is typically observed in conventional Nd-Fe-B sintered magnets. The appearance of the low-field FORC spot indicates that multidomain magnetization reversal is dominant in the as-sintered Ga-doped Nd-Fe-B magnet. On the other hand, the FORC diagram pattern of the annealed Ga-doped Nd-Fe-B magnet at room temperature presents only the high-field FORC spot, which indicates that the single domain magnetization reversal is dominant. This is clearly confirmed using the XMCD microscopy observation. However, with increasing temperature, the FORC diagram pattern of the annealed Ga-doped Nd-Fe-B magnet becomes similar with that of the as-sintered magnet, indicating that the magnetization reversal process of the annealed magnet varies from single domain reversal to multidomain reversal. This change in the magnetization reversal process is well explained from the temperature dependence of the saturation field of the multidomain state, which is evaluated using the remanent initial magnetization curve. The quantitative analysis of the peak top positions of the low-field and high-field FORC spots and their FWHMs are very useful for the deeper understanding of the magnetization reversal behavior of magnets.

We postulate that the above findings and conclusions drawn from the FORC analysis on the Ga-doped Nd-Fe-B magnets could be generally applicable to many permanent magnetic materials, and this method would be very powerful for characterizing the properties of permanent magnets and for understanding the detailed magnetization reversal processes.

Acknowledgments

We gratefully thank Dr. S. Hirosawa for the valuable advice and fruitful discussions. This work was partially supported by Dynamic Alliance for Open Innovation Bridging Human, Environment and Materials from MEXT, the Management Expenses Grants for National Universities Corporations from MEXT, JSPS KAKENHI Grant No. 17H03376, JST, and NIMS Joint Research Hub Program. The XMCD microscopy experiments have been performed at SPring-8 with approval of JASRI (Proposal Nos. 2015A2042, 2015B1998, 2017A1022, and 2017B1028).

References

- 1 J. Fidler, C. Groiss, and M. Tokunaga, The influence of Ga-substitution on the coercivity of Nd-(Fe, Co)-B sintered permanent magnets, *IEEE Trans. Magn.* **29** (1990) 1948-1950.
- 2 J. Bernardi, J. Fidler, M. Seeger, and K. Kronmüller, Preparation and TEM-study of sintered Nd₁₈Fe₇₄B₆Ga₁Nb₁ magnets, *IEEE Trans. Magn.* **26** (1993) 2773-2775.
- 3 A. Tsutai, I. Sakai, T. Mizoguchi, and K. Inomata, Effect of Ga addition to NdFeCoB on their magnetic properties, *Appl. Phys. Lett.* **51** (1987) 1043-1045.
- 4 K. Nakamura and T. Yamazaki, Japan Patent (2015) 5767788.
- 5 T. Sasaki, T. Ohkubo, Y. Takada, T. Sato, A. Kato, Y. Kaneko, and K. Hono, Formation of non-ferromagnetic grain boundary phase in a Ga-doped Nd-rich Nd-Fe-B sintered magnet, *Scr. Mater.* **113** (2016) 218-221.
- 6 M. Soderžnik, H. Sepehri-Amin, T.T. Sasaki, T. Ohkubo, Y. Takada, T. Sato, Y. Kaneko, A. Kato, T. Schrefl, and K. Hono, Magnetization reversal of exchange-coupled and exchange-decoupled Nd-Fe-B magnets observed by magneto-optical Kerr effect microscopy, *Acta Mater.* **135** (2017) 68-76.
- 7 T. Sasaki, T. Ohkubo, and K. Hono, Structure and chemical compositions of the grain boundary phase in Nd-Fe-B sintered magnets, *Scr. Mater.* **115** (2016) 269-277.
- 8 T.T. Sasaki, Y. Takada, H. Okazaki, T. Ohkubo, T. Nakamura, T. Sato, A. Kato, Y. Kaneko, K. Hono, Role of Ga on the high coercivity of Nd-rich Ga-doped Nd-Fe-B sintered magnet, *J. Alloys Compd.* **790** (2019) 750-759.
- 9 H. Sepehri-Amin, T. Ohkubo, T. Shima, and K. Hono, Grain boundary and interface chemistry of an Nd-Fe-B-based sintered magnet, *Acta Mater.* **60** (2012) 819-830.
- 10 T. Kohashi, K. Motai, T. Nishiuchi, and S. Hirosawa, Magnetism in grain-boundary phase of a NdFeB sintered magnet studied by spin-polarized scanning electron microscopy, *Appl. Phys. Lett.* **104** (2014) 232408.
- 11 Y. Murakami, T. Tanigaki, T.T. Sasaki, Y. Takeno, H.S. Park, T. Matsuda, T. Ohkubo, K. Hono, and D. Shindo, Magnetism of ultrathin intergranular boundary regions in Nd-Fe-B permanent magnets, *Acta Mater.* **71** (2014) 370-379.
- 12 T. Nakamura, A. Yasui, Y. Kotani, T. Fukagawa, T. Nishiuchi, H. Iwai, T. Akiya, T. Ohkubo, Y. Gohda, K. Hono, and S. Hirosawa, Direct observation of ferromagnetism in grain boundary phase of Nd-Fe-B sintered magnet using soft x-ray magnetic circular dichroism, *Appl. Phys. Lett.* **105** (2014) 202404.
- 13 K. Hyodo, Y. Toga, A. Sakuma, First-principles study on the magnetic properties of ordered Nd₆(Fe,Ga)₁₄ alloys, *J. Appl. Phys.* **122** (2017) 243904.
- 14 K. Niitsu, A. Sato, T.T. Sasaki, R. Sawada, Y. Cho, Y. Takada, T. Sato, Y.

- Kaneko, A. Kato, T. Ohkubo, D. Shindo, K. Hono, and Y. Murakami, Magnetization measurements for grain boundary phases in Ga-doped Nd-Fe-B sintered magnet, *J. Alloys Comp.* **752** (2018) 220-230.
- 15 C.H. de Groot, K.H.J. Buschow, F.R. de Boer, K. de Kort, Two-powder Nd₂Fe₁₄B magnets with DyGa-addition, *J. Appl. Phys.* **83** (1998) 388-393.
 - 16 Y. Enokido, M. Miwa, S. Goto, Y. Fujikawa, Effects of grain boundary phase on coercivity of dysprosium-free rare earth magnet, *Mater. Trans.* **57** (2016) 1960-1965.
 - 17 X.D. Xu, T.T. Sasaki, J.N. Li, Z.J. Dong, H. Sepehri-Amin, T.H. Kim, T. Ohkubo, T. Schrefl, K. Hono, Microstructure of a Dy-free Nd-Fe-B sintered magnet with 2 T coercivity, *Acta Mater.* **156** (2018) 146-157.
 - 18 K. Miyazawa, S. Okamoto, T. Yomogita, N. Kikuchi, O. Kitakami, K. Toyoki, D. Billington, Y. Kotani, T. Nakamura, T. Sasaki, T. Ohkubo, and K. Hono, First-order reversal curve analysis of a Nd-Fe-B sintered magnet with soft X-ray magnetic circular dichroism microscopy, *Acta Mater.* **162** (2019) 1-9.
 - 19 I.D. Mayergoyz, Mathematical models of hysteresis, *IEEE Trans. Magn. MAG-* **22** (1986) 603-608.
 - 20 R. J. Harrison and J. M. Feinberg, FORCinel: An improved algorithm for calculating first-order reversal curve distributions using locally weighted regression smoothing, *Geochem. Geophys. Geosyst.* **9** (2008) Q05016.
 - 21 C.R. Pike, A.P. Roberts, and K.L. Verosub, Characterizing interactions in fine magnetic particle systems using first order reversal curves, *J. Appl. Phys.* **85** (1999) 6660-6667.
 - 22 C.R. Pike, A.P. Roberts, M.J. Dekkers, and K.L. Verosub, An investigation of multi-domain hysteresis mechanisms using FORC diagrams, *Phys. Earth Planet. Int.* **126** (2001) 11-25.
 - 23 A. Stancu, C. Pike, L. Stoleriu, P. Postolache, and D. Cimpoesu, Micromagnetic and Preisach analysis of the First Order Reversal Curves (FORC) diagram, *J. Appl. Phys.* **93** (2003) 6620-6622.
 - 24 J.E. Davies, O. Hellwig, E.E. Fullerton, G. Denbeaux, J.B. Kortright, and K. Liu, Magnetization reversal of Co/Pt multilayers: Microscopic origin of high-field magnetic irreversibility, *Phys. Rev. B* **70** (2004) 224434.
 - 25 J.E. Davies, O. Hellwig, E.E. Fullerton, J.S. Jiang, S.D. Bader, G.T. Zimányi, and K. Liu, Anisotropy dependence of irreversible switching in Fe/SmCo and FeNi/FePt exchange spring magnet films, *Appl. Phys. Lett.* **86** (2005) 262503.
 - 26 C.R. Pike, C.A. Ross, R.T. Scalettar, and G. Zimanyi, First-order reversal curve diagram analysis of a perpendicular nickel nanopillar array, *Phys. Rev. B* **71** (2005) 134407.
 - 27 J. Yin, H. Zhang, F. Hu, B. Shen, and L.Q. Pan, First order reversal curve

- diagrams of perpendicular magnetic anisotropy films, *J. Appl. Phys.* **106** (2009) 103901.
- 28 V. Bonanni, Y. Fang, R.K. Dumas, C. Zha, S. Bonetti, J. Nogués, and J. Åkerman, First-order reversal curve analysis of graded anisotropy FePtCu films, *Appl. Phys. Lett.* **97** (2010) 202501.
 - 29 N. Sakuma, T. Ohshima, T. Shoji, Y. Suzuki, R. Sato, A. Wachi, A. Kato, Y. Kawai, A. Manabe, and T. Teranishi, Exchange Coupling Interaction in L1₀-FePd/ α -Fe Nanocomposite Magnets with Large Maximum Energy Products, *ACS Nano* **5** (2011) 2806-2814.
 - 30 D. A. Gilbert, G.T. Zimanyi, R.K. Dumas, M. Winklhofer, A. Gomez, N. Eibagi, J. L. Vicent, and K. Liu, Quantitative decoding of interactions in tunable nanomagnet arrays using first order reversal curves, *Sci. Rep.* **4** (2014) 4204.
 - 31 H. Chiriac, N. Lupu, L. Stoleriu, P. Postolache, and A. Stancu, Experimental and micromagnetic first-order reversal curves analysis in NdFeB-based bulk “exchange spring”-type permanent magnets, *J. Magn. Magn. Mater.* **316** (2007) 177-180.
 - 32 T. Schrefl, T. Shoji, M. Winklhofer, H. Oezelt, M. Yano, and G. Zimanyi, First order reversal curve studies of permanent magnets, *J. Appl. Phys.* **111** (2012) 07A728.
 - 33 P.A. Chen, C.Y. Yang, S.J. Chang, M.H. Lee, N.K. Tang, S.C. Yen, and Y.C. Tseng, Soft and hard natures of Nd₂Fe₁₄B permanent magnet explored by first-order-reversal-curves, *J. Magn. Magn. Mater.* **370** (2014) 45-53.
 - 34 T. Yomogita, S. Okamoto, N. Kikuchi, O. Kitakami, H. Sepehri-Amin, T. Ohkubo, K. Hono, T. Akiy, K. Hioki, and A. Hattori, First-order reversal curve analysis in hot-deformed Nd-Fe-B magnets, *Proc. 24th Inter. Workshop on Rare Earth and Future Permanent Magnets and Their Applications (REPM 2016)*, Darmstadt, Germany, 2016, p. 649.
 - 35 T. Yomogita, S. Okamoto, N. Kikuchi, O. Kitakami, H. Sepehri-Amin, T. Ohkubo, K. Hono, T. Akiya, K. Hioki, and A. Hattori, Temperature and field direction dependences of first-order reversal curve (FORC) diagrams of hot-deformed NdFe-B magnets, *J. Magn. Magn. Mater.* **447** (2018) 110-115.
 - 36 Y. Kotani, Y. Senba, K. Toyoki, D. Billington, H. Okazaki, A. Yasui, W. Ueno, H. Ohashi, S. Hirosawa, Y. Shiratsuchi, and T. Nakamura, Realization of a scanning soft X-ray microscope for magnetic imaging under high magnetic fields, *J. Synchrotron Radiat.* **25** (2018) 1444-1449.
 - 37 D. Billington, K. Toyoki, H. Okazaki, Y. Kotani, T. Fukagawa, T. Nishiuchi, S. Hirosawa, and T. Nakamura, Unmasking the interior magnetic domain structure and evolution in Nd-Fe-B sintered magnets through high-field magnetic imaging of the fractured surface, *Phys. Rev. Mater.* **2** (2019) 104413.

- 38 T. Fukagawa and S. Hirosawa, Coercivity generation of surface Nd₂Fe₁₄B grains and mechanism of fcc-phase formation at the Nd/Nd₂Fe₁₄B interface in Nd-sputtered Nd–Fe–B sintered magnets, *J. Appl. Phys.* **104** (2008) 013911.
- 39 S. Bance, B. Seebacher, T. Schrefl, L. Exl, M. Winklhofer, G. Hrkac, G. Zimanyi, T. Shoji, M. Yano, N. Sakuma, M. Ito, A. Kato, and A. Manabe, Grain-size dependent demagnetizing factors in permanent magnets, *J. Appl. Phys.* **116** (2014) 233903.
- 40 J. A. Cape and G. W. Lehman, Magnetic domain structures in thin uniaxial plates with perpendicular easy axis, *J. Appl. Phys.* **42** (1971) 5732-5756.
- 41 S. Chikazumi, Mechanism of high coercivity in rare-earth permanent magnets, *J. Magn. Magn. Mater.* **54-57** (1986) 1551-1555.

Figure Captions

Figure 1 Temperature T dependence of coercivity $\mu_0 H_c$ of the as-sintered (open circle) and the annealed (solid circle) Ga-doped Nd-Fe-B magnets.

Figure 2 (a) Reversal curves and (b) FORC diagram of the as-sintered Ga-doped Nd-Fe-B magnet measured at RT. The blue and red lines indicate the low-field and high-field FORC spot regions, respectively. The color bar indicates the normalized value of ρ in the FORC diagram.

Figure 3 Reversal curves and FORC diagrams of the annealed Ga-doped Nd-Fe-B magnet. (a) and (b) are the results measured at RT, (c) and (d) at 100 °C, and (e) and (f) at 200 °C. The blue and red lines indicate the low-field and high-field FORC spot regions, respectively. The color bar indicates the normalized value of ρ in the FORC diagram.

Figure 4 (a) XMCD demagnetization curve of the annealed Ga-doped Nd-Fe-B magnet. The black dots denote the magnetization curve by VSM. (b)-(g) XMCD images taken with the demagnetization field varying from 3 to -2 T, corresponding to the encircled data points in (a). The grains rimmed by black and white lines in (b)-(g) are the inter-grain and intra-grain fractured grains, respectively.

Figure 5 (a) XMCD reversal magnetization curve corresponding to the high-field FORC spot of the annealed Ga-doped Nd-Fe-B magnet. The black dots and gray denote the reversal and demagnetization curves by VSM. (b)-(g) XMCD images taken with the field varying from -1.6 to 1.8 T, corresponding to the encircled data points in (a). The grains rimmed by black and white lines in (b)-(g) are the inter-grain and intra-grain fractured grains, respectively.

Figure 6 Upper images are the color maps of the SD reversed, MD reversed, and unreversed grains of each $\mu_0 H_r$. The grains rimmed by black and white lines are the inter-grain and intra-grain fractured grains, respectively. Lower graph shows the histogram of these SD reversed, SD reversed, and unreversed grain numbers as a function of $\mu_0 H_r$.

Figure 7 (a) Initial and remanent initial magnetization curves of the annealed Ga-doped Nd-Fe-B magnet measured at RT. Inset shows the relationship

between the data points on the two magnetization curves. (b) Saturation field $\mu_0 H_s^i$ and $\mu_0 H_s^r$ of the initial and remanent initial magnetization curves of the as-sintered and annealed Ga-doped Nd-Fe-B magnet as a function of temperature T . $\mu_0 H_c$ is also plotted for comparison.

Figure 8 (a) and (b) are the reversal curves and the FORC diagram of the as-sintered Ga-doped Nd-Fe-B magnet, respectively, measured at RT as graphical examples of peak top positions and FWHM of the low-field and high-field FORC spots. (c) and (d) are the peak fields along the H_r - and H -axes $\mu_0 H_{p,r}^{L(H)}$ and $\mu_0 H_p^{L(H)}$, respectively, as a function of temperature T . (e) and (f) are the FWHM along the H_r - and H -axes $\mu_0 \Delta H_r^{L(H)}$ and $\mu_0 \Delta H^{L(H)}$, respectively, as a function of temperature T . Superscripts of L and H denote those for low-field and high-field FORC spots.

Table I

Sample	As-sintered	Annealed	
Temperature	RT	RT	200 °C
$\mu_0 H_s^i$ (T)	0.37	0.28	0.19
$\mu_0 H_s^{col}$ (T)	0.53	0.41	0.27

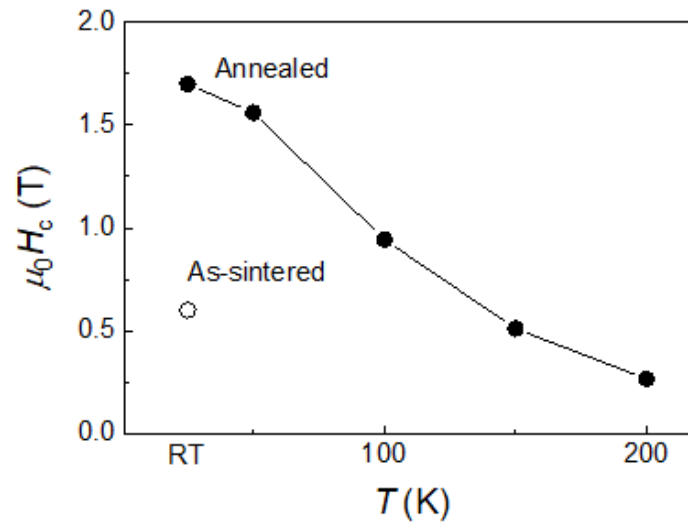


Fig.1

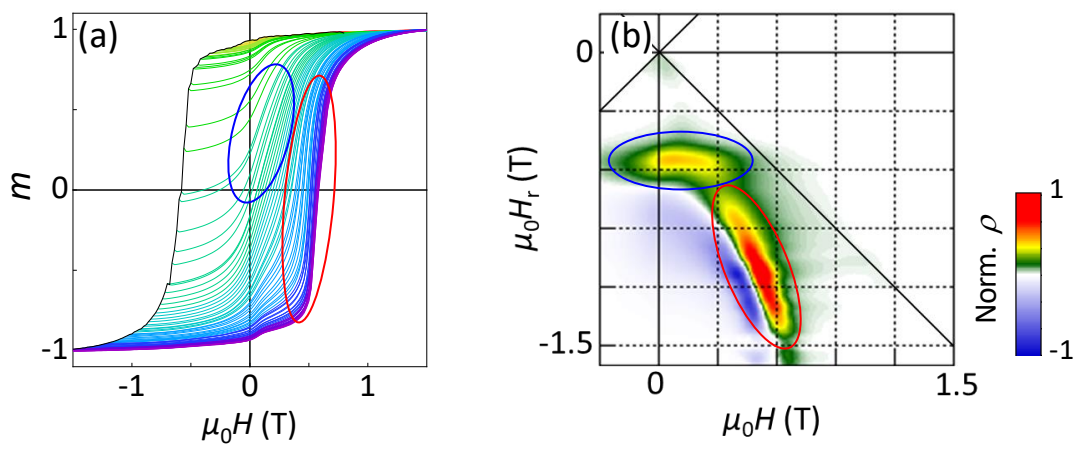


Fig.2

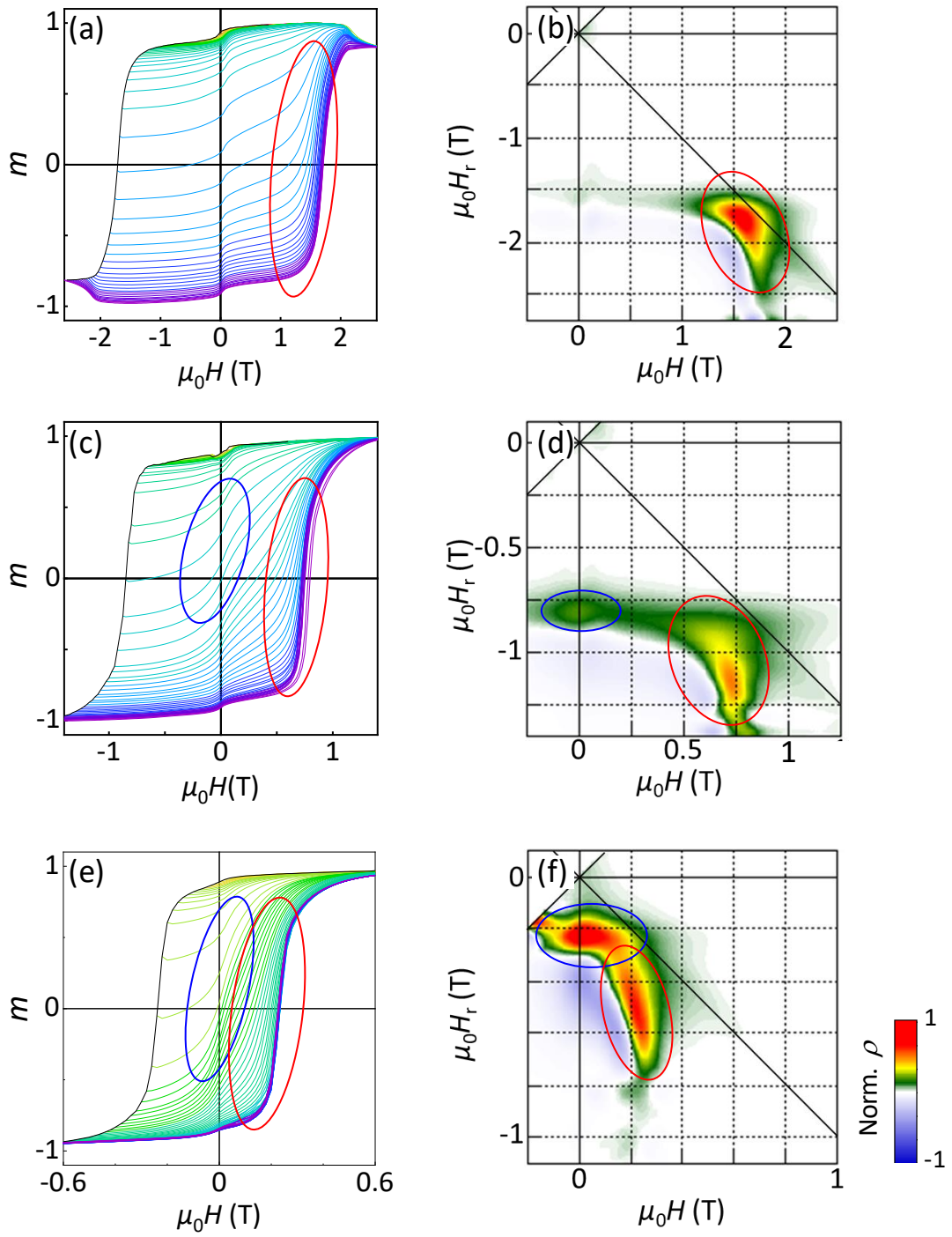


Fig.3

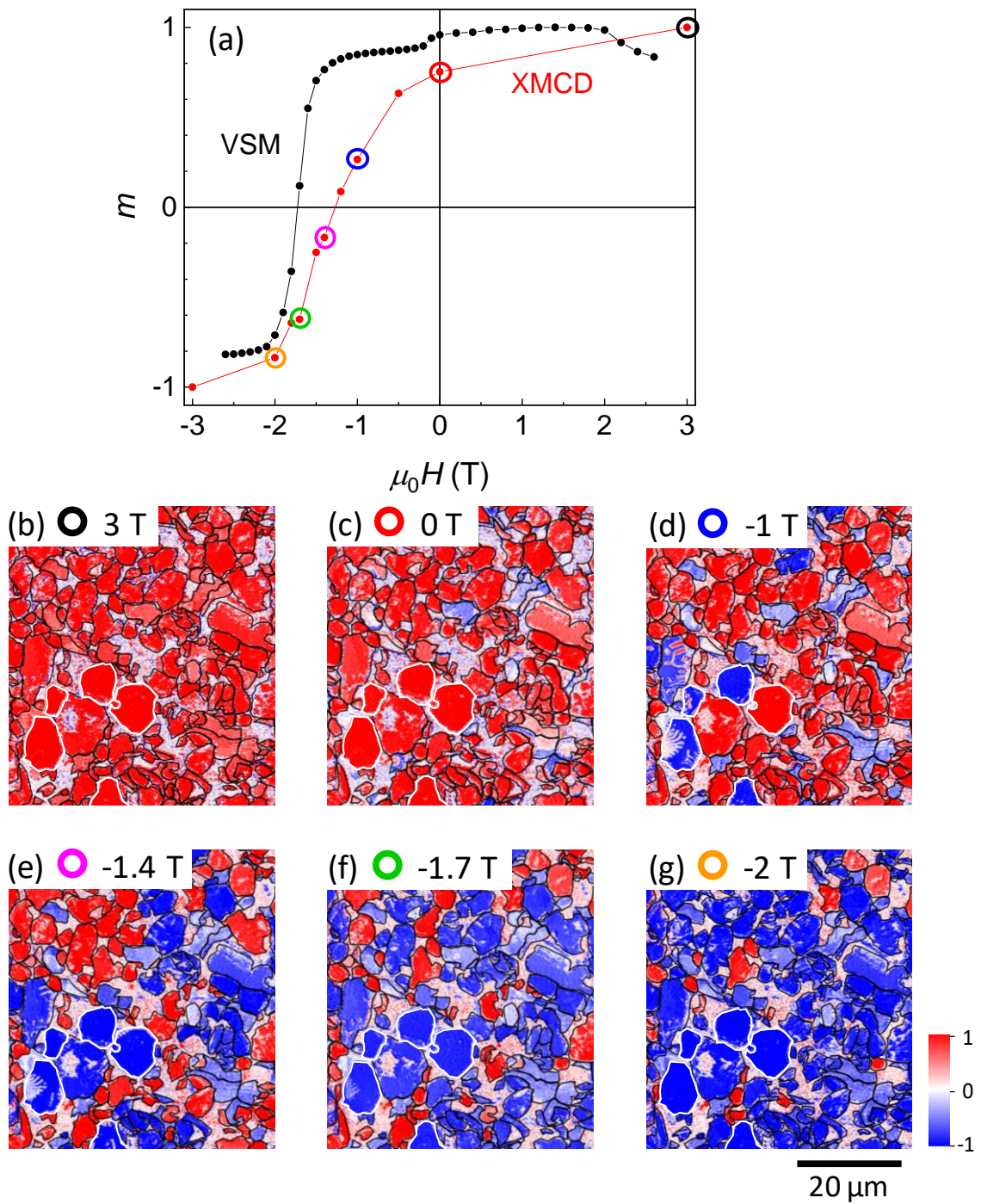


Fig.4

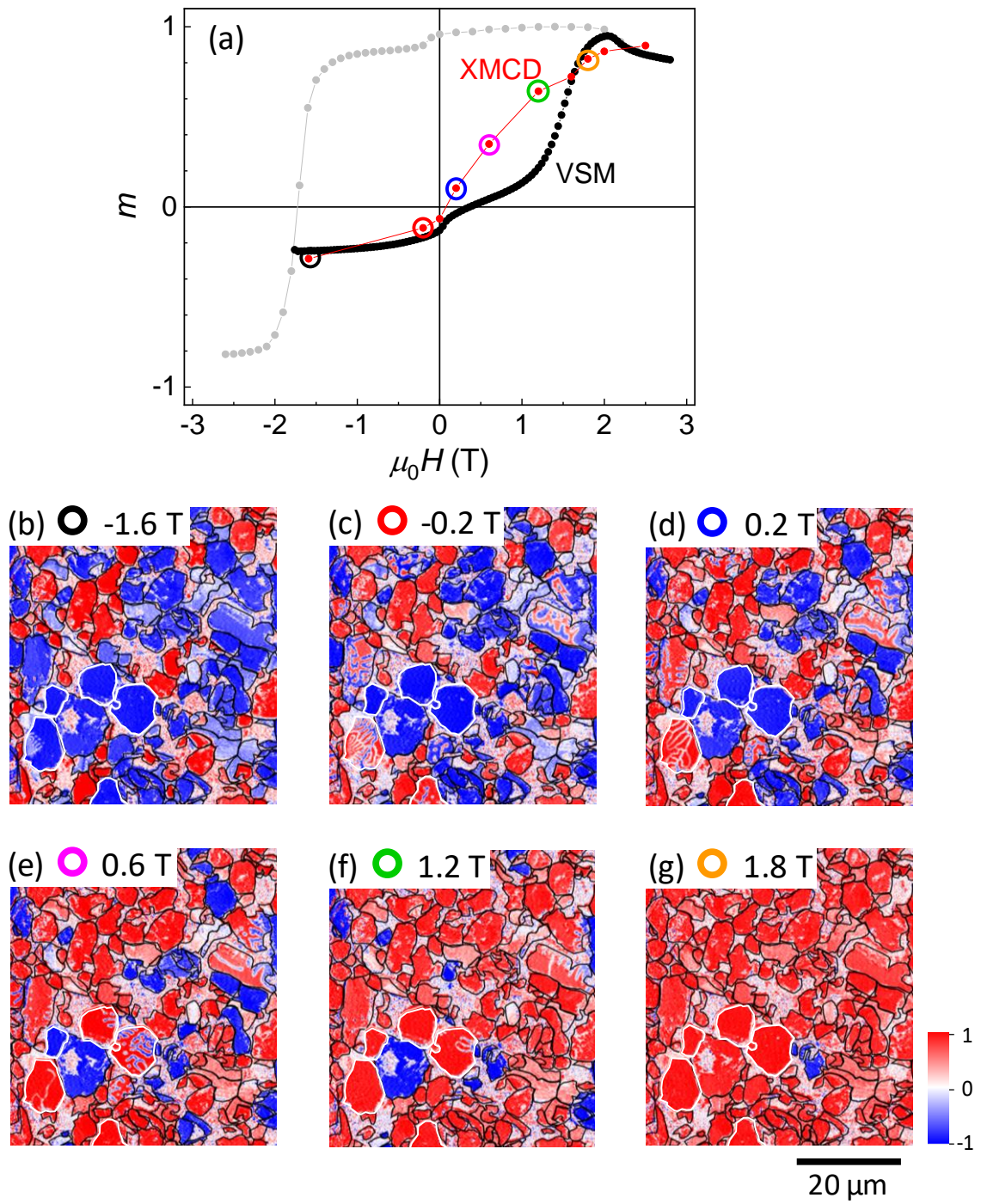


Fig.5

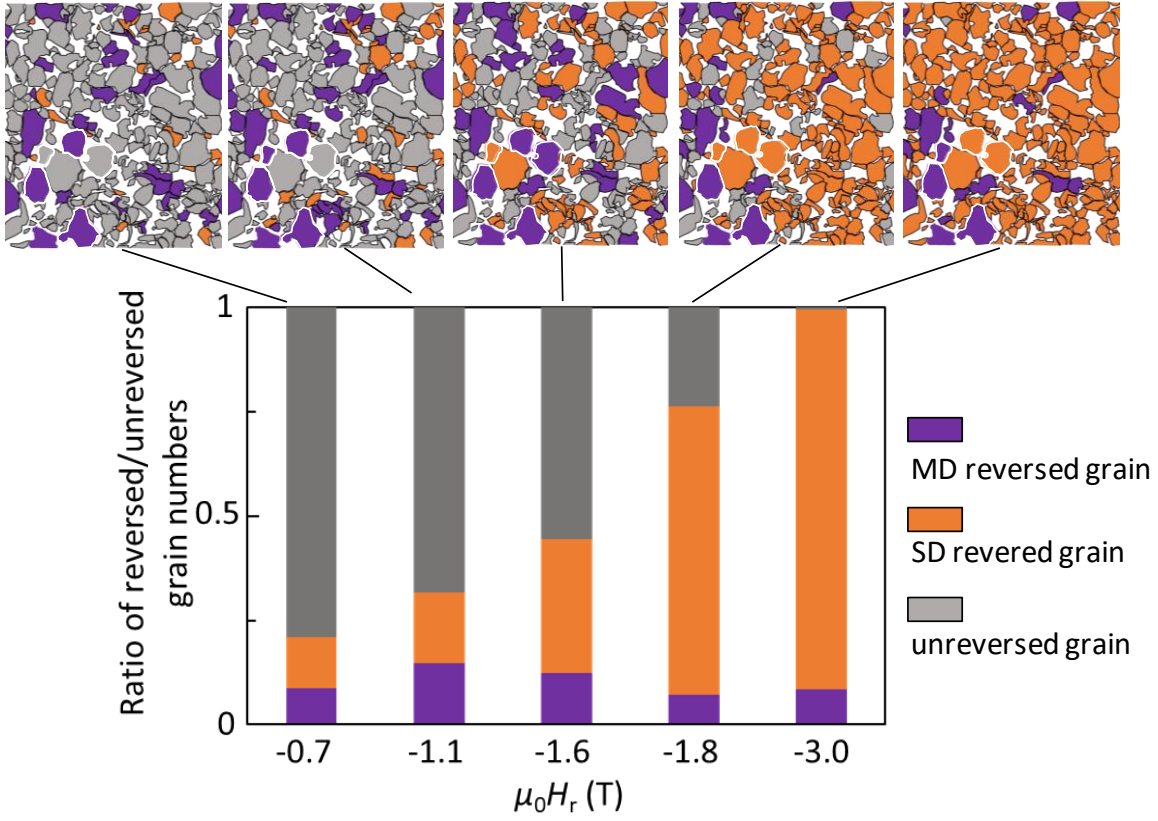


Fig.6

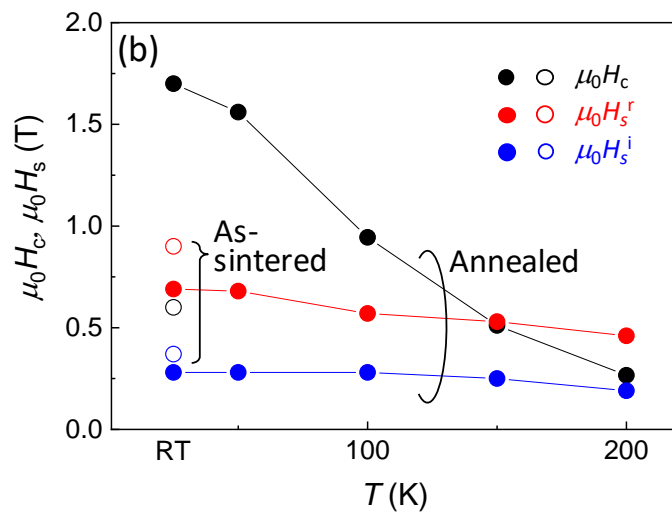
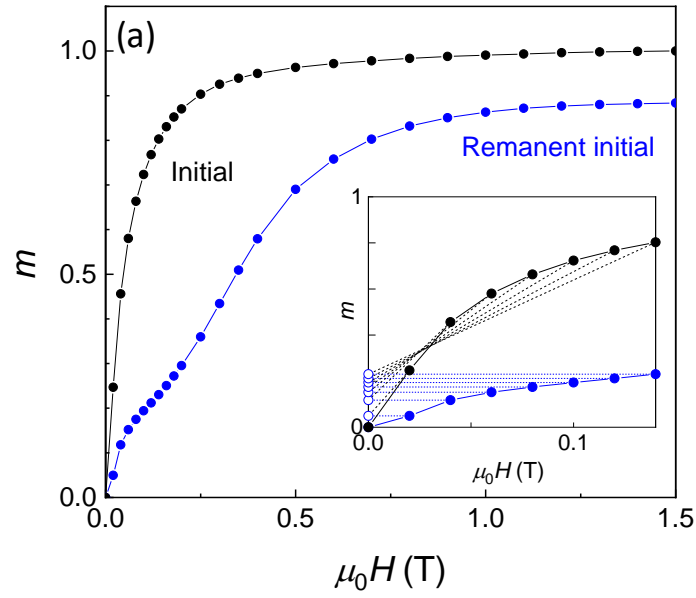


Fig.7

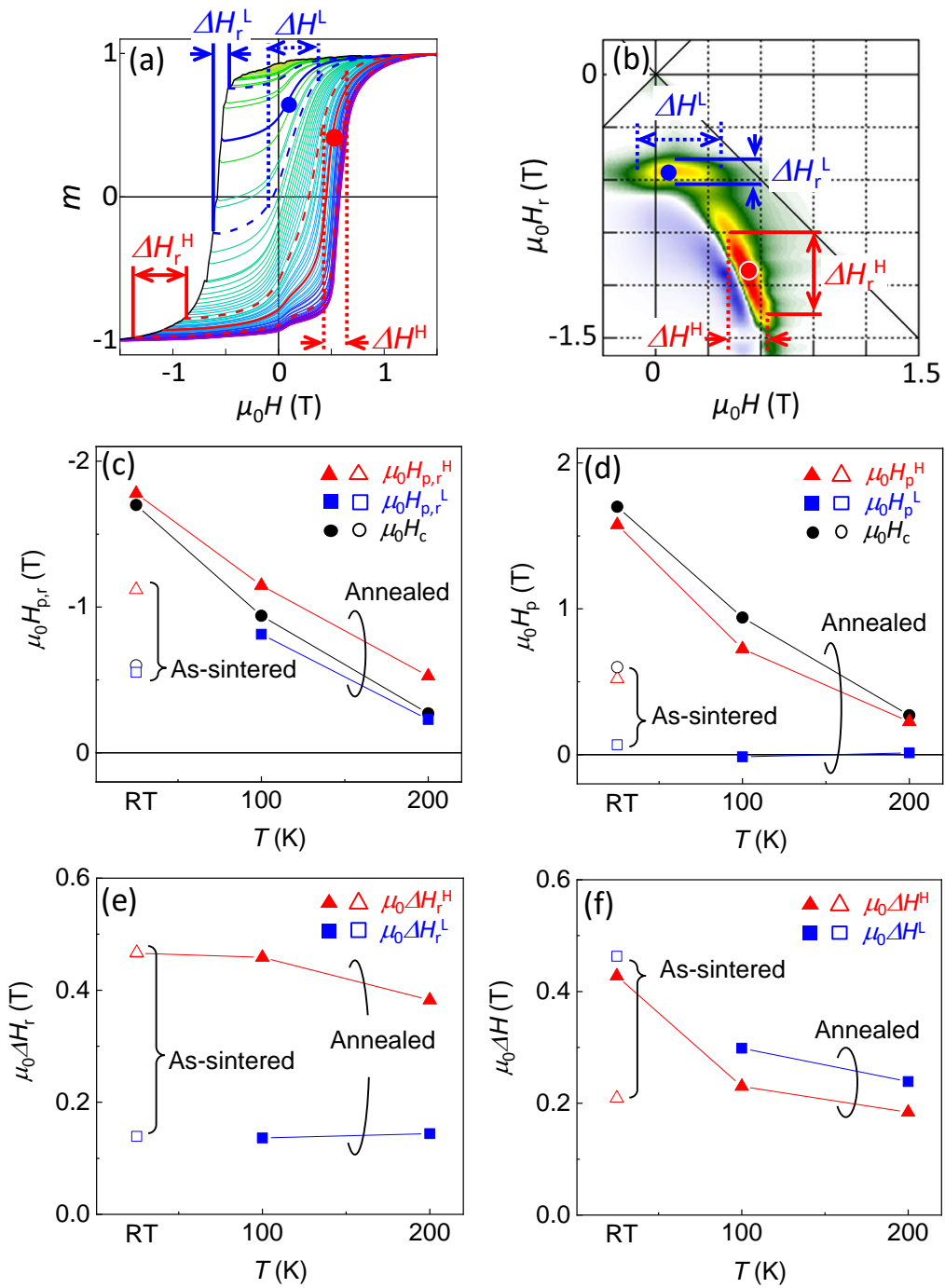


Fig.8